


Ion Doped Hollow Silica Nanoparticles as Promising Oligonucleotide Delivery Systems to Mesenchymal Stem Cells

Chloe Trayford, Dina M Ibrahim, Sabine van Rijt 

MERLN Institute for Technology-Inspired Regenerative Medicine, Maastricht University, Maastricht, MD, 6200, the Netherlands

Correspondence: Sabine van Rijt, Department of Instructive Biomaterials Engineering, MERLN Institute for Technology-Inspired Regenerative Medicine, Maastricht University, P.O. Box 616, MD, Maastricht, 6200, the Netherlands, Email s.vanrijt@maastrichtuniversity.nl

Introduction: Oligonucleotide (ON) therapy is a promising treatment for a wide range of complex genetic disorders, but inefficient intracellular ON delivery has hindered clinical translation. Hollow silica nanoparticles (HSN) hold potential as effective ON delivery vehicles since ON can be encapsulated in the hollow core in situ where they are protected from degradation by eg nucleases. However, HSN must be modified to allow degradation and subsequent (sub)cellular ON release. In this report, we investigated the use of ion and fluorescent dye co-doping in the HSN silica matrix to enable HSN degradability and in vitro visualization.

Methods: HSN were core encapsulated with ON, doped with Ca^{2+} , Cu^{2+} , Zn^{2+} , Se^{2+} and Sr^{2+} ions and co-condensed with rhodamine b isothiocyanate (RITC) by a modified reverse microemulsion method. HSN were physiochemically characterized and their biological activity such as uptake and toxicity were evaluated in mesenchymal stem cells (hMSCs).

Results: We successfully doped HSN with RITC and Ca^{2+} , Cu^{2+} , Zn^{2+} and Sr^{2+} ions. We observed that doping HSN with Ca^{2+} and Sr^{2+} enhanced RITC incorporation while ON encapsulation in HSN increased Cu^{2+} and Zn^{2+} doping efficiency. Moreover, our dual-doped HSN demonstrated controlled ON release in the presence of intracellular mimicking levels of glutathione (GSH) and limited release in the absence of GSH over 14 days. HSN were biocompatible in hMSCs up to 300 $\mu\text{g}/\text{mL}$ except for Cu^{2+} doped HSNs which were cytotoxic even at $\sim 10 \mu\text{g}/\text{mL}$. HSN uptake was influenced by the dopant ion, DNA encapsulation, and HSN concentration, where Zn-HSN showed the lowest and Sr-HSN and Se-HSN_D, the highest uptake in hMSCs.

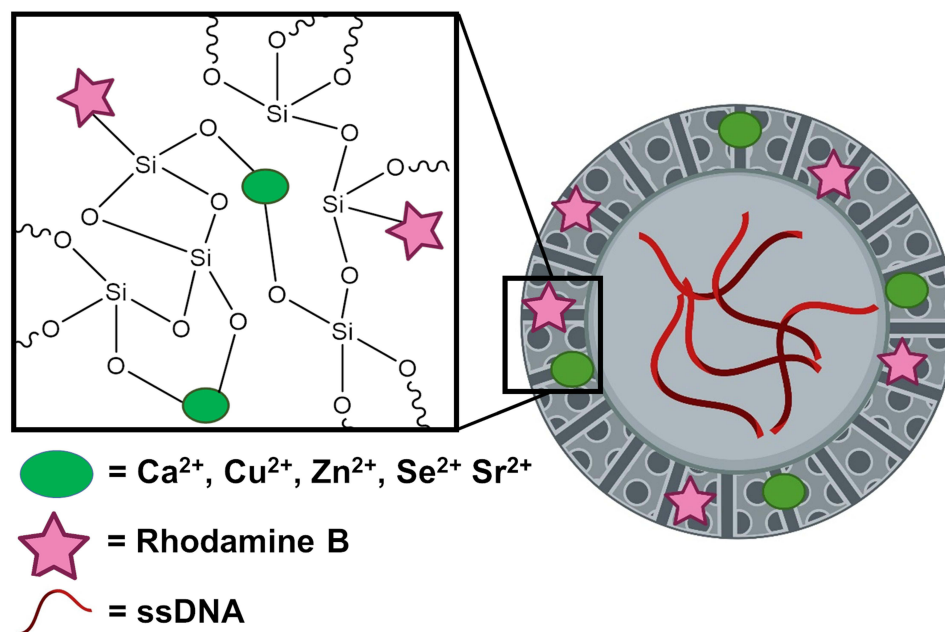
Conclusion: We report a straightforward one-pot procedure to create ion and fluorescent dye co-doped HSN that can efficiently incorporate ON, as promising new gene vectors.

keywords: hollow silica nanoparticles, ion-doping, oligonucleotide therapy, intracellular specific degradation, controlled delivery

Introduction

Oligonucleotides (ON) hold potential to treat a vast array of pathologies ranging from influenza to neurodegenerative disorders, as well as various rare genetic diseases. ON are short fragments of DNA or RNA that mostly bind via complementary Watson–Crick base pairing.¹ As such, ON therapeutics can be designed to target genes simply with knowledge of their primary sequence. These ON can bind to genes encoding pathogenic proteins to block or modify their expression, leading to drastically improved patient prognoses. In contrast, conventional small molecule protein therapeutics require extensive, often repetitive screening efforts and optimization. Thus, ON allows precise and personalized treatment that overcomes major challenges of small molecule drugs such as off-target toxicity and “undruggable” proteins.² Recently, a surge in approved mRNA vaccines such as those produced to tackle COVID-19 has demonstrated the wide-reaching potential of ON therapies.³ Still, significant hurdles remain that halt their clinical translation, most of which concern ON characteristics such as inability to be cell internalized, instability, and susceptibility to degradation. The development of ON delivery vehicles such as viral vectors has enabled ON cell uptake and offered protection against degradation, but immunotoxicity of the carriers has thwarted their therapeutic development.⁴

Graphical Abstract



Nanoparticles (NP) have been proposed as alternative ON vehicles owing to their high loading capacities and ability to bypass immunorecognition.⁵ Of the different NP for gene delivery, inorganic NP based on silica and calcium phosphate such as large pore mesoporous silica (LPMSN), bioactive glass (MBGN) and hydroxyapatite NPs (HANP) have demonstrated high gene transfer abilities.^{6–8} For example, HANP have excellent biocompatibility, degradability, and ON encapsulation efficiency due to the high affinity of ON with calcium.⁹ Luo et al, demonstrated that KRAS-siRNA loaded HANP showed similar in-vitro transfection efficiency compared to commercial agents, effectively downregulating KRAS protein expression in the treatment of pancreatic cancer.⁸ LPMSN have also been widely used for ON therapy owing to the high carrying capacity of the enlarged mesopores and modification possibilities that increase ON loading.⁶ However, these and most other NPs require ON to be loaded on the NP surface, meaning they are exposed to nucleases, and their release is hard to control. This poses significant problems such as ON degradation and premature delivery, leading to inefficient transfection and off-target toxicity.

One way to circumvent this issue is by using hollow silica nanoparticles (HSN), which are composed of a non-degradable mesoporous silica shell and a hollow cavity in the center. Large biomolecules such as enzymes can be loaded within the hollow core of HSN to enable intracellular enzyme therapy.^{10–12} For instance, Chang et al synthesized horseradish peroxidase encapsulated HSN, which were internalized in cancer cells, and converted prodrug indole-3-acetic acid to cytotoxic radicals to promote cell apoptosis.¹⁰ There is only a couple of examples where HSN were investigated for gene delivery purposes. In these examples, ON was complexed on the nanoparticle surface, and the core was loaded with small molecule drugs such as doxorubicin or photosensitizers.^{13,14} We recently reported the first HSN systems with core encapsulated ON that displayed controlled ON release as a function of HSN degradation by intracellular GSH.¹⁵ This was achieved by co-condensation of RITC-APTES and glutathione degradable organosiloxane (triethoxysilyl) propyl]tetrasulfide (BTES) in the silica matrix. We could also functionalize the surface for subcellular targeting of the mitochondria.

In the present study, we synthesized HSN doped with various cations and investigated their effect on DNA encapsulation efficiency and HSN degradability. Ion doping introduces structural defects in the silica matrix and has been used in the mesoporous silica NP (MSN) field to not only increase MSN degradation but also introduce imaging

capabilities and bioactivity.^{16,17} For example, doping MSN with calcium, zinc or strontium increases degradability leading to expulsion of Ca^{2+} , Zn^{2+} or Sr^{2+} , which can promote new bone formation (osteogenesis) in hMSC as well as effective renal clearance.^{17,18} Further, copper or selenium-doped MSN have been shown as effective anti-cancer agents due to MSN degradation and release of cytotoxic Cu^{2+} and Se^{2+} .^{19,20} Ion-doped MSN have also shown higher loading efficiencies towards negatively charged ON than un-doped MSN.²¹ As such, we hypothesize that ion doping of HSN can promote silica shell degradation, endow NPs with additional bioactive properties, and improve ON loading efficiency. In this study, the silica matrix of HSN was dual doped with RITC and Calcium (Ca^{2+}), Copper (Cu^{2+}), Zinc (Zn^{2+}), Selenium (Se^{2+}), Strontium (Sr^{2+}), Manganese (Mn^{2+}) or Magnesium (Mg^{2+}) ions. We then compared the morphology and surface charge of HSN with DNA-encapsulated HSN. We also investigated the relationship between dopants by analyzing the ion, fluorophore, and DNA incorporation efficiency of all HSN formulations. Further, we evaluated the biocompatibility and uptake of HSN in hMSC. Overall, dual ion- fluorophore doped, DNA encapsulated HSN were developed as an interesting new class of traceable, bioactive ON carrier systems with modifiable surfaces for gene therapeutic applications.

Materials and Methods

Materials

Water was purified using a Milli-Q system at a conductivity of $18.2 \text{ M}\Omega \text{ cm}^{-1}$ (Millipore, US). ssDNA-FAM with sequence: 6'FAM-5'-GGGTTTAAACCCGGGTTTAA-3', $\text{CaCl}_2 \cdot 2\text{H}_2\text{O}$, $\text{Cu}(\text{NO}_3)_2 \cdot 3\text{H}_2\text{O}$, ZnCl_2 , $\text{Na}_2\text{O}_3\text{Se}$, $\text{SrCl}_2 \cdot 6\text{H}_2\text{O}$, $\text{MnCl}_2 \cdot 4\text{H}_2\text{O}$ and $\text{MgCl}_2 \cdot 6\text{H}_2\text{O}$, Triton X100, Rhodamine B isothiocyanate (RITC), 98% 3-aminopropyltriethoxysilane (APTES), cyclohexane, 1-hexanol, Igepal CA-630, Tetraethyl orthosilicate (TEOS) and 100% Ethanol were purchased from Sigma-Aldrich (Merck Life Sciences NV, NL). Aqueous ammonium (28–30 wt%), 60 V/V% Nitric acid (HNO_3), 37 V/V% hydrochloric acid (HCl), 2 mL glass screw-top vials (SureSTART™) and standard solutions of silicon, scandium, calcium, copper, zinc, selenium and strontium for inductively coupled plasma mass spectroscopy (ICP-MS) (10 mg/L, ARISTAR) were purchased from VWR (NL). a-MEM growth medium, penicillin–streptomycin (P/S), phosphate-buffered saline (PBS) were purchased from Gibco. Fetal bovine serum (FBS) was obtained from Bodingco B.V. 96 MicroWell Polystyrene Plate and 0.05% trypsin-0.01% EDTA was purchased from ThermoFisher Scientific (NL). CellTiter 96® AQueous Non-Radioactive Cell Proliferation Assay kit (MTS) was purchased from Promega (USA). Gelatin from porcine skin was obtained from Sigma-Aldrich. Ninety-six wellplates with glass bottom were purchased from Greiner Bio-One. Paraformaldehyde was obtained from Fisher Scientific. Triton X-100 and tween-20 were purchased from Merck. Bovine serum albumin (BSA) was obtained from Carl Roth. Alexa Fluor™ 647 phalloidin was purchased from Invitrogen. 4',6 diamidino-2-phenylindole (DAPI) was obtained from Sigma Aldrich.

HSN Synthesis and Characterization

HSN doped with RITC and bioactive ions were synthesized with adaption of a previously reported protocol.¹⁵ RITC-APTES was prepared as previously reported.²² Different solutions of ionic compounds at 200 mg/mL were formed by dissolving 20 mg $\text{CaCl}_2 \cdot 2\text{H}_2\text{O}$, $\text{Cu}(\text{NO}_3)_2 \cdot 3\text{H}_2\text{O}$, ZnCl_2 , $\text{Na}_2\text{O}_3\text{Se}$, $\text{SrCl}_2 \cdot 6\text{H}_2\text{O}$, $\text{MnCl}_2 \cdot 4\text{H}_2\text{O}$ and $\text{MgCl}_2 \cdot 6\text{H}_2\text{O}$ in 100 μL water. Reverse microemulsion systems were made with cyclohexane (19.06 mL, 176 mmol) Igepal CA-520 (5 g, 15 mmol), and n-hexanol (3 mL, 24 mmol) and stirred for 10 min in a round bottom flask. Then, TEOS (100 μL , 0.48 mmol), RITC-APTES (25 μL , 0.0023 mmol), and water (350 μL) were added to the mixtures. For synthesis of HSN doped with ions at 10 mol % different volumes of as-prepared ionic solutions; Ca^{2+} (56.8 μL), Cu^{2+} (58.1 μL) Zn^{2+} (32.7 μL), Se^{2+} (40.5 μL), Sr^{2+} (64 μL), Mg^{2+} (48.8 μL) or Mn^{2+} (47.5 μL) were made up to 350 μL and added to the emulsion system instead of water. Further, to encapsulate DNA in ion-doped HSN, DNA-FAM (70 μL , 250 μM) was added to the same volumes of ionic solutions as for ion-doped HSN, made up to 350 μL and similarly added instead of water. After stirring the emulsions in the dark for 2 h, ammonia (250 μL , 28–30 wt%) was added and kept at RT under vigorous stirring for 36 h. To isolate the silica NP, ethanol (80 mL) was added to the microemulsion solution and the product collected by centrifugation ($3217 \times g$, 25 min, 10°C). Then, to remove excess surfactant, NP were washed twice in ethanol. To remove the core, solid nanospheres were stirred in 100 mL water at 50°C overnight. HSNs were then collected by centrifugation ($3217 \times g$, 25 min, 10°C) and the pellet was dispersed in a 25 mL

mixture of ethanol/water (v/v=70/30). The HSNs were stored at -20°C for up to 6 months. Morphological characterization was performed by transmission electron microscopy (TEM) using a FEI Tecnai electron microscope. To prepare HSN for TEM imaging, suspensions (5 μL , 0.3 mg/mL) were spotted on a 200 mesh carbon grid and air dried at RT overnight. To determine HSN size distribution, 50 hSN were analyzed using the particle analysis function on ImageJ. Electrokinetic potential (ζ) was measured using the Malvern Zetasizer Nano (Malvern Panalytical, UK) at 25°C at an angle of 90° where NPs were suspended in water at a concentration of 0.3 $\mu\text{g/mL}$.

HSN Doping Efficiency

To assess the RITC and DNA-FAM concentration of HSN, RITC and DNA-FAM standard curves were made in the range of 0 to 2.5 μM . Fluorescence quantifications were performed using a CLARIOstar spectrophotometer equipped with MARS data analysis software (BMG LABTECH, DE). HSN were measured with RITC and DNA-FAM standard curves in a 96 well plate in triplicate at 100 $\mu\text{g/mL}$. The fluorescent signal for DNA-FAM was detected at $\lambda_{\text{ex}}=488\text{ nm}$ and $\lambda_{\text{em}}=521\text{ nm}$ and for RITC at $\lambda_{\text{ex}}=560\text{ nm}$ and $\lambda_{\text{em}}=595\text{ nm}$. The total element composition of each HSN was measured using ICP-MS (iCaP Q, Thermo Scientific, US) and a scanning electron microscope (SEM) coupled to EDX (JSM-IT200, JEOL, US). To prepare samples for ICP-MS, aqua regia (AR, HCl: HNO_3 , molar ratio 3:1) was added to HSN dried in glass vials for a w/v; 0.5 mg/500 μL . HSN were degraded overnight at 40°C using an ultrasonic bath (Bransonic, Fisher Scientific) and purified by centrifugation (21,300 $\times g$, 5 min, 20°C). The collected pellet was dissolved in NaOH (0.1 M, 100 μL) and sonicated (3 h, 40°C). Next, a matrix solution was freshly prepared by dissolving 500 ppb scandium in 1% HCl. Digested HSN (200 μL from AR and 100 μL from NaOH homogenate) were diluted 1:10 in the as-prepared matrix (300 μL : 2700 μL matrix). Additionally, a multi-element standard curve from 0.39 to 100 $\mu\text{g/L}$ Si^{4+} and from 0.04 to 10 $\mu\text{g/L}$ Ca^{2+} , Cu^{2+} , Zn^{2+} , Se^{2+} , and Sr^{2+} was made by dilution of ionic stock solutions in the as-prepared matrix. The element amount in each sample was extrapolated from concentration curves and calculated as a percentage of Si content. For EDX analysis, HSN were spotted on an aluminum specimen stub and for each sample, three spectra were recorded at random locations.

DNA-FAM Release and HSN Degradation

The release kinetics of DNA-FAM from HSN were determined by measuring DNA concentration in the supernatant of HSN samples in the presence or absence of 3 mm glutathione (GSH) at different time points. Each HSN with encapsulated DNA-FAM was dispersed in PBS at a concentration of 1 mg/mL in the presence or absence of 3 mm GSH and incubated in a ThermoMixer[®] C (Eppendorf, DE) (500 rpm, 37°C). After 0 h, 6 h, 1 d, 4 d, 7 d and 14 d, 100 μL of solution was removed from each sample in triplicate. The HSN/HSN remnants were isolated from solution by centrifugation (21,300 $\times g$, 5 min, RT) and the supernatant was collected. DNA-FAM concentration in the supernatant was measured using a Nanodrop (Witec AG, CH). The corresponding HSN pellets were resuspended in ultrapure water and spotted for TEM (HSN Synthesis and Characterization).

HSN Biocompatibility and Uptake

Human mesenchymal stem cells derived from bone marrow (hMSCs) were obtained from Promocell (C-12974). hMSCs were expanded in freshly prepared α -MEM supplemented with 10% FBS, 1% P/S and were kept at 5% CO_2 in a humidified atmosphere at 37°C . hMSCs medium was refreshed 24 h post seeding then every 2–3 days. hMSCs culture was used at approx. 80% confluence at passage 4. To assess hMSCs metabolism after HSN exposure, the MTS assay was conducted according to the manufacturer's guidelines. In brief, hMSCs were seeded at 3000 cells/ cm^2 in 96 well plates. hMSCs were exposed to HSN for 24 h at concentrations 10, 50, 100, and 300 $\mu\text{g/mL}$ in triplicate. In each plate 20 control wells were included, 15 without HSN (cells only) and 5 without both cells and HSN (medium only). After 24 h, excess HSN were removed by washing cells twice with PBS. Then, to each well, 80 μL of medium and 20 μL of MTS/PMS solution (2 mg/mL/ 0.92 mg/mL, 20:1 v/v) was added and the plates were incubated for 3 h in 5% CO_2 at 37°C . The absorbance was read at 490 nm using a CLARIOstar spectrophotometer. Assessment of the HSN uptake with done via flow cytometry and inverted fluorescence microscopy imaging. Flow cytometry ((BD Accuri C6, DE) was performed to quantitatively assess cellular uptake of HSN, flow cytometry. hMSCs were seeded at 2000 cells/ cm^2 in 12 well plates, to

ensure even cell coverage the plate was moved sporadically. Then, hMSCs were exposed to HSN at 10 $\mu\text{g}/\text{mL}$ or 100 $\mu\text{g}/\text{mL}$. After 24 h, cells were washed twice with PBS, trypsinized, and resuspended in 300 μL PBS on ice. For each measurement, 5000 cells were gated. FlowJo (V10, LLC) was used for data analysis. For fluorescence microscopy, cells were seeded (3000 cells/ cm^2) in 96 well plates with glass bottom coated with 0.1% gelatin from porcine skin to promote cellular adhesion. When cells were 80% confluent, media was replaced with media containing HSN with a concentration of 100 $\mu\text{g}/\text{mL}$ for 24 h. Following, media containing HSN was removed, cells were washed 3 \times in PBS then fixed in 4% paraformaldehyde for subsequent staining and imaging.

Inverted Fluorescence Microscopy Imaging for HSN Uptake

Following cells fixation, they were permeabilized with 0.5% Triton X-100 in PBS (v/v) for 10 min. Next, blocking was done through incubating different samples in 3% BSA (w/v) in 0.1% PBS tween-20 (v/v) for 1 h to minimize background staining. F-actin was stained with Alexa Fluor™ 647 phalloidin diluted 1:500 in 1% BSA in 0.1% PBS-20 tween for 2 h. Nuclei were counterstained with 4',6 diamidino-2-phenylindole (DAPI). Finally, samples were washed 3x in PBS followed by imaging using Nikon Eclipse Ti-E microscope (Nikon Instruments Europe BV, the Netherlands). Images were captured as Z stacks with a step size of 0.5 μm and reconstructed into 3D images using ImageJ software. Only one Z stack with high resolution and was selected as well as a 3D cross section to show the proximity of the HSN to nuclei and actin filaments.

Statistics

Results are expressed as a mean \pm SD (standard deviation). Statistical analysis was performed using GraphPad PRISM (GraphPad Software, US). One way ANOVAs and post hoc analysis were used for comparison among groups. Results were considered statistically significant at $p < 0.05$.

Results and Discussion

Synthesis and Characterization of Ion-Doped Fluorescent HSN

HSN were synthesized by a reverse micro-emulsion approach, where the addition of water to bulk oil phases formed water-in-oil (w/o) droplets that were the reaction centers of silica condensation. Ions were doped in the HSN matrix in situ by replacing water with ionic solutions to incorporate ions into siloxane bonds during silica condensation. Further, to enable fluorescent tracing of HSN, the dye-siloxane conjugate, RITC-APTES was also doped in the silica matrix by co-condensation. Following this procedure, eight types of HSN dual doped with RITC and the following ions; Ca^{2+} (Ca-HSN), Cu^{2+} (Cu-HSN), Zn^{2+} (Zn-HSN), Se^{2+} (Se-HSN), Sr^{2+} (Sr-HSN), Mn^{2+} (Mn-HSN) and Mg^{2+} (Mg-HSN), were formed. HSN with RITC but without ion doping were also synthesized as control particles (cHSN).

Ca-HSN, Cu-HSN, Zn-HSN, Se-HSN, and Sr-HSN were spherical in morphology with a hollow core. However, variable core hollowness, homogeneity and diameter was observed by TEM imaging (Figure 1). In contrast, Mg-HSN and Mn-HSN formed solid NPs that were heterogeneous in size and were not further used in the study (Figure S1). This indicates that for certain ions, HSN synthesis is disrupted, and ion choice is an important design criterion. Cu-HSN and Zn-HSN were the same size as cHSN, likely due to the similar ionic radii and electronegativity of Cu^{2+} and Zn^{2+} compared to Si^{4+} and similar binding modes to oxygen ($\sim 91.1 \pm 4.9$ nm, Figure 2a). It was unsurprising therefore that doping with the larger ion Ca produced HSN with increased size compared to cHSN, Cu-HSN and Zn-HSN (Ca-HSN: 106.7 ± 10.8 nm, $p < 0.0001$, Figure 2a). However, increasing the radii of the ion dopant further (Se^{2+} or Sr^{2+}) produced HSN smaller than cHSN (Se-HSN: 77.5 ± 7.0 nm and Sr-HSN: 67.8 ± 11.7 nm, $p < 0.0001$). Similar observations were made in the bioactive glass field, where doping with 5% Ag produced smaller MBGNs than both un-doped and 5% Cu-doped MGBNs.²³ Ion incorporation can proceed via different bonding mechanisms (ionic as opposed to covalent) when the radii surpass a certain size. This has previously been observed for MSN doped with lanthanide ions.^{24,25}

Zeta potential analysis showed that the surface charge of all ion-doped HSN were negative and not significantly different to cHSN ($\sim -11.0 \pm 7.6$ mV, Figure 2b), indicating the dispersal of ions in the aqueous phase, which upon silica nucleation at the w/o interface were contained to the HSN core.^{26,27}

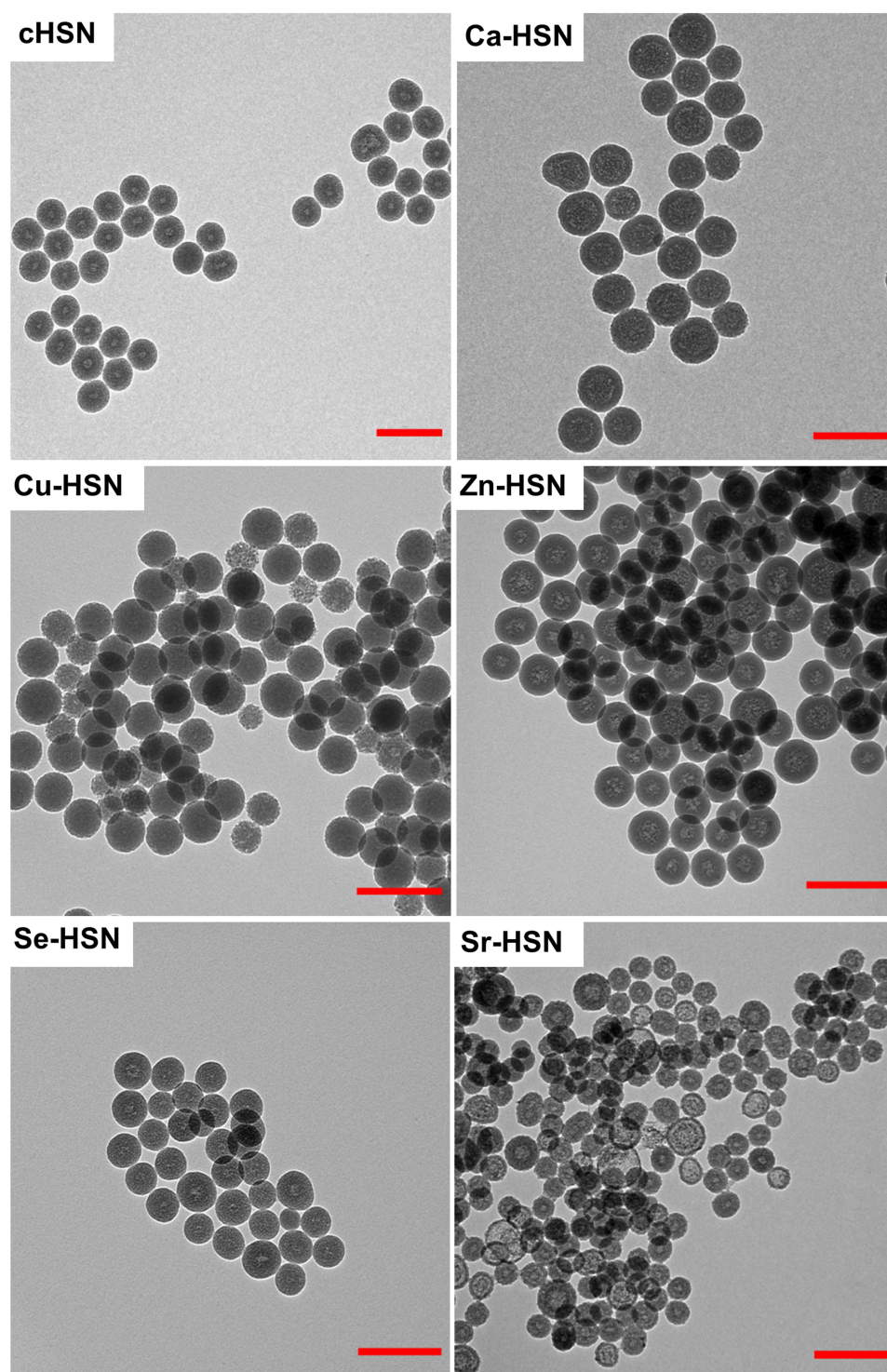


Figure 1 TEM micrographs of cHSN, Ca-HSN, Cu-HSN, Zn-HSN, Se-HSN and Sr-HSN showing round morphology and hollow or semi-hollow cores.

RITC doping in the HSN matrix was quantified by fluorescence analysis and ion doping by EDX and ICP-MS. cHSN, Cu-HSN, Zn-HSN and Se-HSN contained similar RITC-APTES despite steric competition of ions and RITC indicating that dopant limits were not yet reached (Figures 2c, S2; $\sim 0.33 \pm 0.04 \mu\text{M}$ RITC in $100 \mu\text{g/mL}$). In contrast, Ca-HSN and Sr-HSN contained significantly higher concentrations of RITC ($0.99 \pm 0.02 \mu\text{M}$ and $0.73 \pm 0.27 \mu\text{M}$, respectively). This was probably a result of the increased binding strength of alkaline earth metals with aryl carboxylates compared to

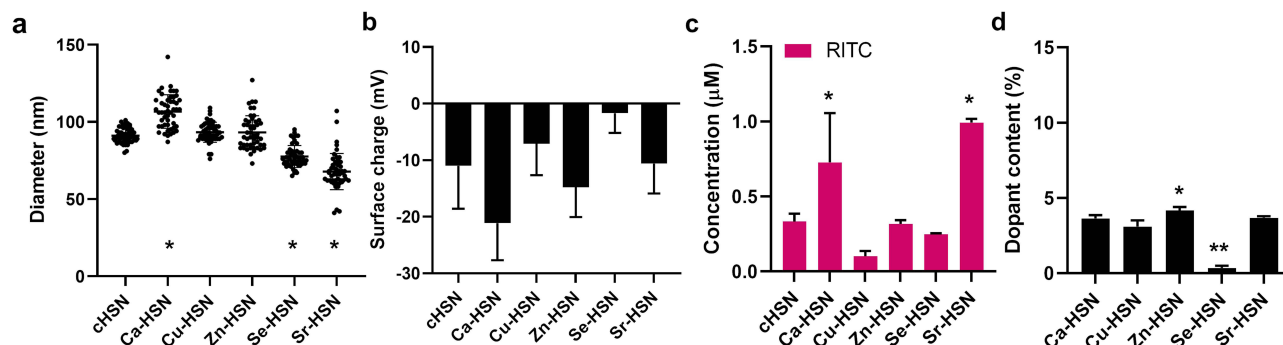


Figure 2 NP characterization of cHSN, Ca-HSN, Cu-HSN, Zn-HSN, Se-HSN and Sr-HSN. (a) Size analysis of 50 HSN by Image J (b) Zeta potential analysis. (c) RITC concentration in 100 µg of NP as determined by fluorescence analysis. (d) Ion doping efficiency in Ca-HSN, Cu-HSN, Zn-HSN, Se-HSN and Sr-HSN calculated by ICP-MS analysis. Statistical significance is determined compared to HSN for (a and c) where * $p < 0.0001$ or each sample in (d) where * $p < 0.001$ and ** $p < 0.0001$.

transition metal ions.^{28–30} ICP-MS and EDX analysis further revealed successful ion doping in all HSN (Figures 2d, S3). Different ion doping efficiencies were observed by ICP-MS analysis. Specifically, the ion doping efficiencies in Ca-HSN, Cu-HSN and Sr-HSN were not significantly different ($\sim 3.7 \pm 0.2\%$, Figure 2d), while Se content in Se-HSN was significantly lower ($0.3 \pm 0.1\%$, $p < 0.0001$, Figure 2d). The highest ion doping amount was observed in Zn-HSN which contained $4.2 \pm 0.3\%$ Zn ($p < 0.0395$, Figure 2d).

Although ion-doped solid silica NP have been synthesized previously by w/o microemulsion,^{26,31–33} we are the first to successfully synthesize w/o microemulsion HSN doped with Ca^{2+} , Cu^{2+} , Zn^{2+} , Se^{2+} , and Sr^{2+} ions. For all HSN except Se-HSN, we were able to incorporate between 3.1 and 4.2 mol % ions, which was much higher than what has previously been reported for doped w/o microemulsion silica NP (0.7 mol %).²⁶ We observed that Ca^{2+} and Sr^{2+} doping in HSN could increase the incorporation efficiency of RITC and brightness of HSNs, which may be a promising strategy to allow higher resolution in cell tracing and sensing applications.³⁴

DNA Incorporation in Ion-Doped Fluorescent HSN

Next, we investigated whether we could incorporate single-stranded 20 bp DNA in the hollow cores of Ca-HSN, Cu-HSN, Zn-HSN, Se-HSN and Sr-HSN in a one-pot synthesis. To simultaneously encapsulate DNA and dope the HSN matrix with bioactive ions and RITC, DNA was first mixed with ionic solutions, which was added to the bulk oil phase including RITC which formed the aqueous reaction centers for HSN formation. Six DNA encapsulated NP were formed; un-doped (cHSN_D) and HSN doped with Ca^{2+} (Ca-HSN_D), Cu^{2+} (Cu-HSN_D), Zn^{2+} (Zn-HSN_D), Se^{2+} (Se-HSN_D) and Sr^{2+} (Sr-HSN_D). The synthesized HSN were characterized by TEM and Image J analysis (Figure 3 and 4a).

DNA incorporated HSNs, cHSN_D, Ca-HSN_D, Zn-HSN_D, and Se-HSN_D, were smaller than unloaded HSN (Figures 4a, S4) which was likely a result of DNA compaction by electrostatic complexation with positive ions and/or RITC-APTES. DNA compaction has been observed with a range of positively charged species especially divalent cations such as Ca^{2+} and Mg^{2+} by effectively neutralizing DNA charge and reducing inter-strand repulsion.^{35–37} Further, complexation of positive APTES with DNA likely creates a nucleation site for the condensation of TEOS, which has been previously observed in the synthesis of DNA-templated silica structures.^{38,39} As such, we expect the size of our HSN to be governed by the size of compacted DNA. Zeta potential analysis revealed that DNA encapsulation in Se-HSN_D, Cu-HSN_D, Zn-HSN_D, and Sr-HSN_D did not affect the surface charge (Figures S5, 2b, 4b). Successful RITC doping and DNA-FAM incorporation in all NP was confirmed by fluorescence analysis (Figure 4c). However, Cu^{2+} , Zn^{2+} and Sr^{2+} doped HSN contained lower amounts of DNA than un-doped, Ca^{2+} and Se^{2+} doped HSN, with an encapsulation efficiency ranging from $5.6 \pm 0.3\%$ (Zn-HSN_D) to $32.7 \pm 2.0\%$ (cHSN_D) (Figure S6). It is likely that our one-pot synthesis system causes steric competition between DNA, ions and RITC-APTES. This phenomenon could also account for the decreased RITC doping efficiency observed when DNA was encapsulated in Ca-HSN and Sr-HSN (Figure S7). Nevertheless, Ca-HSN_D contained the highest DNA content of all our ion doped HSN. This is likely explained by the high affinity of Ca^{2+} with DNA,⁴⁰ which has previously been for siRNA loading in Ca^{2+} doped MSN.²¹

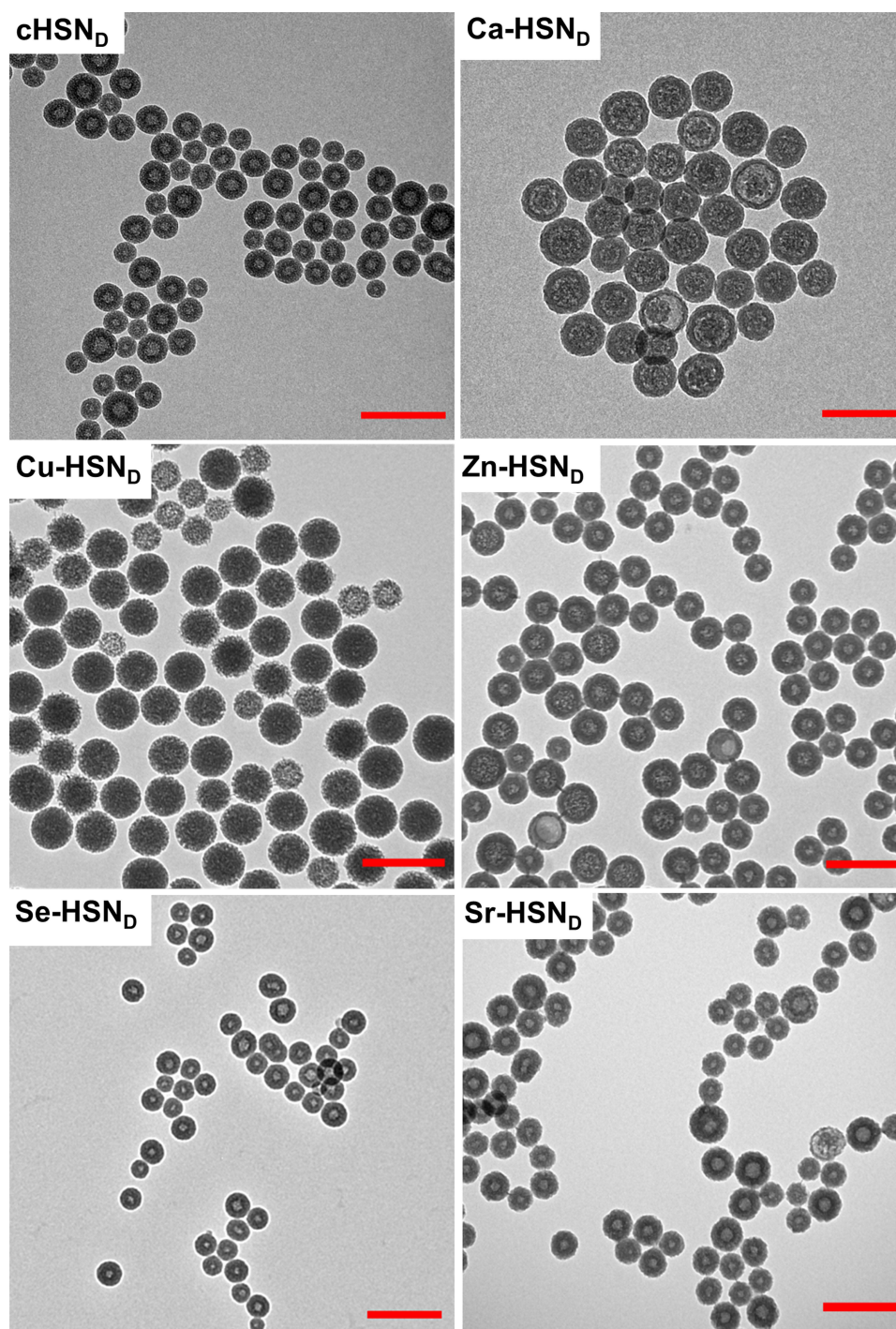


Figure 3 TEM micrographs of cHSN_D, Ca-HSN_D, Cu-HSN_D, Zn-HSN_D, Se-HSN_D and Sr-HSN_D showing round morphology and hollow cores.

In general, our Cu-HSN displayed exceptional properties upon DNA encapsulation compared to cHSN, Ca-HSN, Zn-HSN, Sr-HSN and Se-HSN. For example, the Cu content of Cu-HSN increased 3-fold to $11.6 \pm 2.1\%$, while the ion doping efficiency of our other HSN did not change, likely a result of the relatively high binding affinity of Cu^{2+} and DNA ($p < 0.0001$, [Figures 2d](#), [S8](#), [4d](#)). This was similarly observed by Hackl et al who showed that DNA binding saturation could be achieved with lower concentrations of Cu^{2+} than Ca^{2+} and Mn^{2+} .⁴¹ We also showed that Cu-HSN_D was larger than Cu-HSN, which was probably due to increased Cu^{2+} doping efficiency ($p < 0.01$, [Figure S4](#)). This was also observed in the MSN field where larger NP were formed with increasing copper dopant content.⁴² However, for these MSN, Cu^{2+}

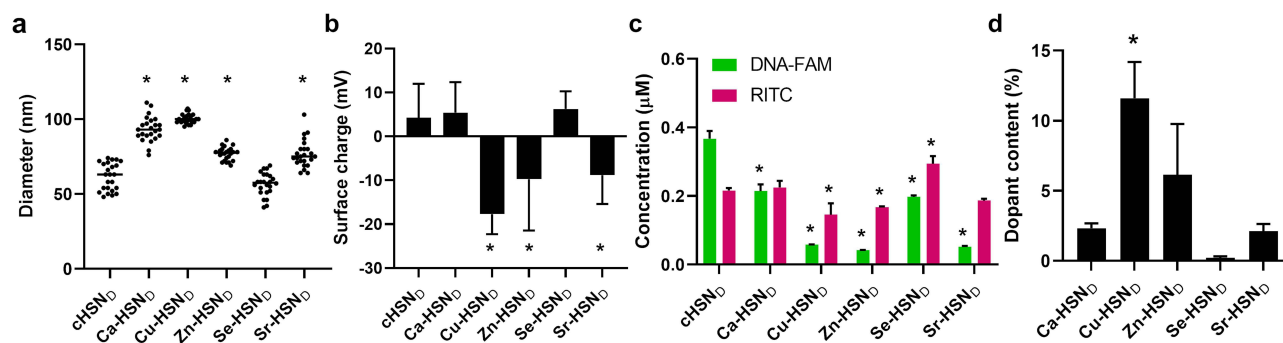


Figure 4 Characterization of amount of DNA encapsulated, and efficiency of RITC and bioactive ion doping in HSN. (a) Size analysis of 50 HSN by Image J. (b) Zeta potential analysis. (c) Concentration of RITC and DNA-FAM in 100 µg of HSN as determined by fluorescence analysis. (d) Ion doping efficiency in Ca-HSN_D, Cu-HSN_D, Zn-HSN_D, Se-HSN_D and Sr-HSN_D calculated by ICP-MS analysis. Statistical significance is determined compared to cHSN_D for (a) or each sample for (c and d) where *p<0.0001.

doping was limited to 5 mol %, while our Cu-HSN_D achieved Cu²⁺ doping greater than 10 mol %. Thus, we propose DNA binding as a useful strategy to modulate the copper content of silica NP and as such, their bioactivity.

Here, we adapted our fluorescent HSN to incorporate DNA in situ. We observed that DNA encapsulation significantly affected the size, surface charge, and RITC and ion doping efficiencies of HSN. Although we previously demonstrated the synthesis of fluorescent HSN with encapsulated DNA, ion doping and its effect on HSN physiochemical properties was not investigated.¹⁵ Understanding the effect of ion doping is crucial to allow HSN optimization since small changes in NP properties have been shown to significantly impact cell interaction and transfection efficacy.^{43,44} In contrast to sol-gel synthesis, our one-pot method of HSN formation allows dopants and DNA to freely interact, which likely also causes DNA compaction. Several studies have demonstrated that compaction can reduce DNA susceptibility to degradation, as well as regulate or improve cell transfection efficiency.^{36,45} Further, our procedure forms HSN, dopes with RITC and ions as well as loads DNA in the core all within a single synthetic step. Previous examples of HSN gene vectors required multiple steps to synthesize HSN and anchor ON to the HSN surface.^{13,14} For example, Lin et al developed light responsive HSN vectors synthesized by formation, surface grafting, immobilization of a light responsive linker and pDNA condensation.¹⁴ Our one-pot HSN system reduces production time, costs as well as batch-to-batch variability associated with lengthy synthetic procedures.

Release Kinetics of ON

Next, ON release from cHSN_D, Ca-HSN_D, Cu-HSN_D, Zn-HSN_D, Se-HSN_D, and Sr-HSN_D in PBS or 3 mM GSH were measured over 14 d (Figure 5). We observed that the DNA release rate depended on ion dopant type and the presence of GSH. Maximum DNA release from cHSN_D was reached after 7 d in GSH, while release from Ca-HSN_D, Zn-HSN_D, Se-HSN_D, and Sr-HSN_D occurred at or before 3 d (Figure 5). It is likely that the ion doping leads to defects in the silica matrix, increasing nanoparticle degradation and subsequent DNA release. Although we only focus here on DNA release profiles, the entrapment of DNA in the hollow core means that release is proportional to the rate of HSN degradation and ion expulsion. Pohaku Mitchell et al, similarly showed that HSN doped with 5.7% iron ions demonstrated complete cargo and ion release after 7 d due to NP degradation.⁴⁶ The quickest DNA release rate was observed for Cu-HSN_D, where maximum release occurred after 6 h. Cu-HSN_D also showed high accumulative DNA release ~10-fold higher than the other tested HSN (46.4 ± 0.5 nmol, Figures 5c, S9). It is known that Cu²⁺ can bind to DNA and enhance as well as shift its absorbance to longer wavelengths due to increased $\pi \rightarrow \pi^*$ transition between DNA bases.⁴⁷ Accumulative release profiles of cHSN_D, Zn-HSN_D, Se-HSN_D, and Sr-HSN_D reached totals between 4.5 and 6.8 nmol DNA. Ca-HSN_D showed the highest maximum release of 6.8 nmol, which was likely a result of high ON incorporation (Figure 5d-f).

For all HSN, gradual DNA release in the presence of GSH and limited release in the absence of GSH was observed, possibly due to accelerated HSN degradation by reduction with GSH. TEM imaging revealed little morphological changes to HSN in the presence of GSH, except for a slight increase in porosity (Figures 6, S10, S11). Several studies have shown that silica NP etching occurs initially at the core and pore walls, leading to cavity coalescence and cargo

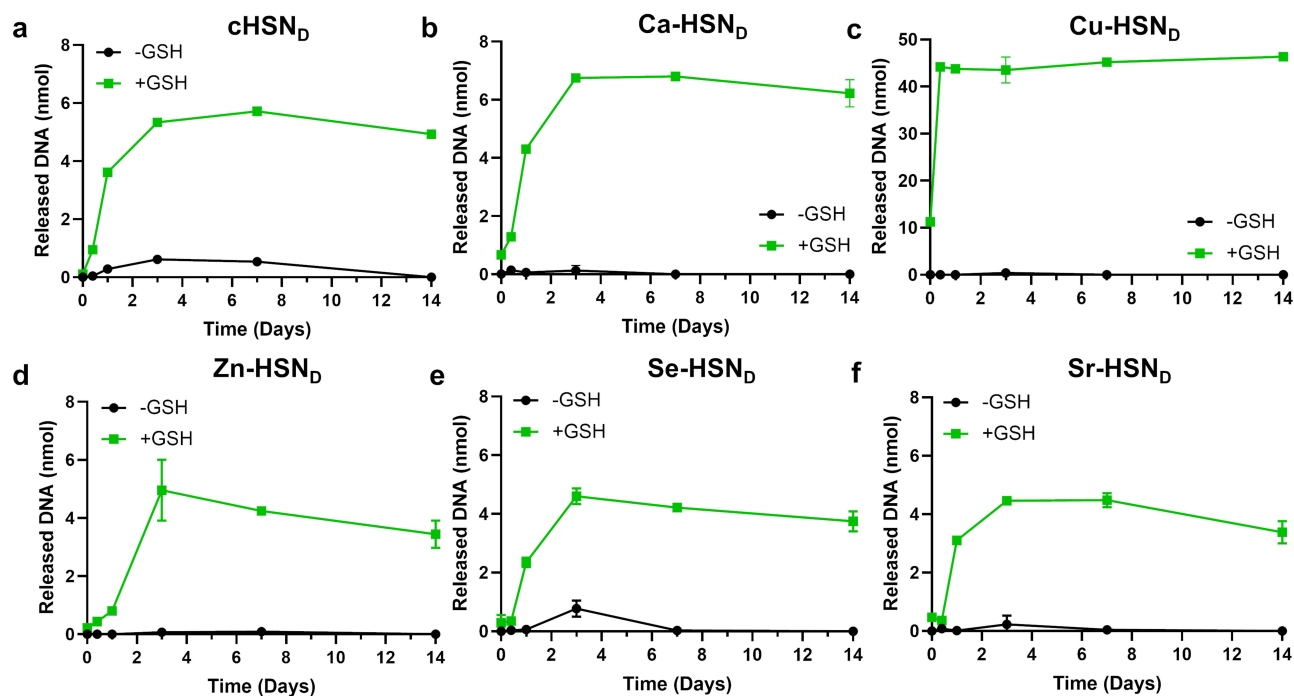


Figure 5 Release kinetics of our DNA encapsulated HSN in 0 mM (-GSH) or 3 mM GSH (+GSH) at timepoints: 0 hr, 6 hr, 1 d, 3 d, 7 d, 14 d. (a) cHSN_D, (b) Ca-HSN_D, (c) Cu-HSN_D, (d) Zn-HSN_D, (e) Se-HSN_D and (f) Sr-HSN_D. Error bars are derived from biological triplicates.

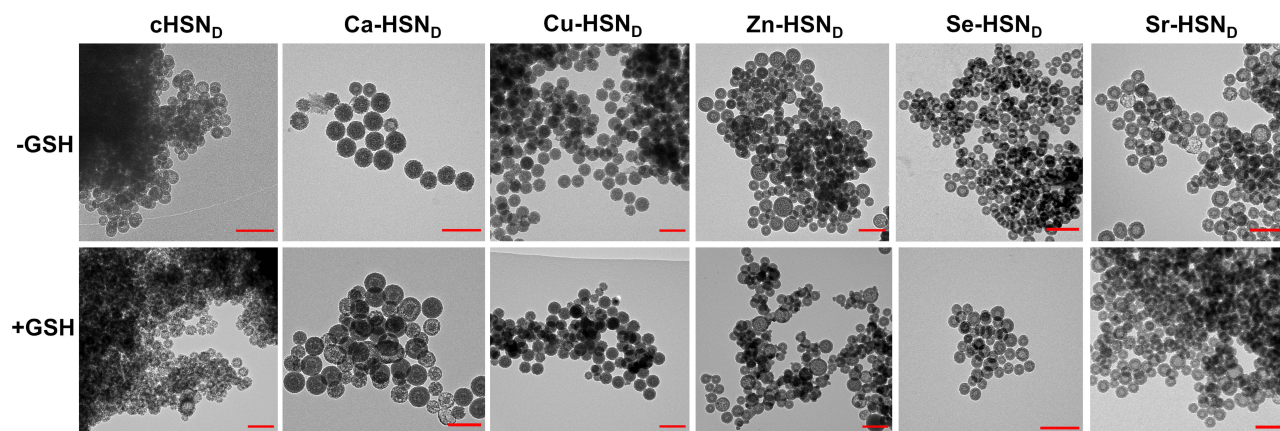


Figure 6 TEM images showing morphology of HSN after 3 d incubation in PBS at 37 degrees in the presence or absence of GSH. Scale bars = 200 nm.

release.^{48,49} Thus, depending on DNA size, it is likely that only partial degradation is needed to allow DNA release from the hollow core.

All our HSN formulations showed similar DNA release profiles between 3 and 7 d in intracellular mimicking conditions. Previous examples demonstrated ON release upon stimulation, but these strategies required multiple post-functionalizations to anchor ON to the HSN surface.^{13,14} For example, Lin et al, developed HSN capable of light mediated ON release by immobilizing a light responsive linker at the surface followed by condensation of pDNA, which required 5 synthetic steps. Our one-pot HSN system negates the need for multiple complex surface modifications. Further, surface functionalization of ON often leads to burst ON release upon stimulation.¹⁴ Longer, consistent release profiles as observed with our HSN_D could increase the efficacy of ON therapy by constantly stimulating cells throughout the cell cycle. This was previously shown by Vandembroucke et al, who developed an ON carrier formed of slowly degrading poly (beta-amino ester) that was able to extend gene silencing over the 5-d period of NP degradation.⁵⁰ Further, tailoring the ON release timeframe for different cells could

also increase transfection efficiency. This was demonstrated by Dobek et al, where a predictive model of transfection efficiency showed cell cycle to be a limiting factor.⁵¹

DNA release from our HSN was dependent on the presence of GSH, likely due to HSN degradation in these conditions (Figures 6, S11). Several studies have shown that mesoporous silica degrades faster when dispersed in mediums with high ionic strength.^{48,49,52,53} For example, Rodriguez-Ramos et al, found that MSN dispersed in PBS at 37°C degraded almost entirely after 12 h while degradation in water was negligible.⁵² Further, it has been shown that doped silica NP are more susceptible to degradation and cargo release in slightly acidic, reducing solutions.^{54,55} GSH mediated degradation of ON encapsulated HSN likely enables intracellular specific DNA release due to high intracellular (1–10mM) and low extracellular (10µM) GSH levels.⁵⁶ As such, our HSN systems prevent extracellular ON release that is linked to off-target effects and reduced transfection efficiency.

Uptake and Biocompatibility of Ion-Doped HSN

Next, the biocompatibility and intracellular uptake of all HSN formulations were investigated in hMSCs. hMSCs were exposed to 10–300 µg/mL doped HSN with and without DNA and the metabolic activity was assessed using an MTS assay. hMSCs metabolic activity was unaffected after exposure to cHSN, Ca-HSN, Se-HSN, Sr-HSN, cHSN_D, Ca-HSN_D, Zn-HSN_D, Se-HSN_D, and Sr-HSN_D at all tested HSN concentrations (Figure 7a). However, incubation of hMSC with Cu-HSN and Cu-HSN_D at concentrations >10 µg/mL led to a decrease in cell metabolic activity. For example, after exposure

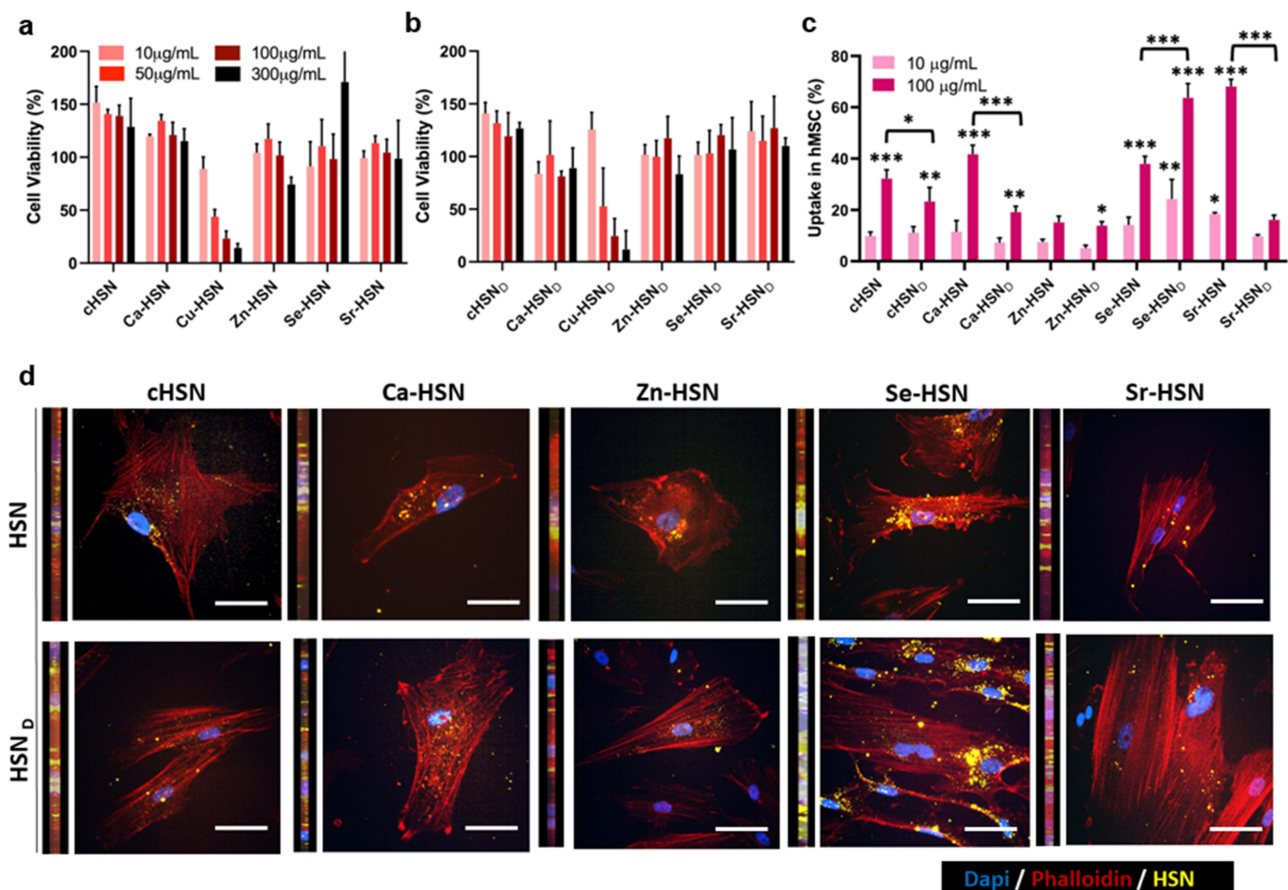


Figure 7 hMSCs metabolic activity and uptake of developed HSN. Metabolic activity of hMSCs was conducted after 24 h exposure to 10, 50, 100 and 300 µg/mL of (a) cHSN, Ca-HSN, Cu-HSN, Zn-HSN, Se-HSN, Sr-HSN and (b) cHSN_D, Ca-HSN_D, Cu-HSN_D, Zn-HSN_D, Se-HSN_D and Sr-HSN_D. Viability is expressed as a percentage of unlabeled cell viability. (c) Uptake of HSN in hMSCs was determined by flow cytometry after 24 h exposure with at HSN formulations at both 10 and 100 µg/mL. (d). Representative fluorescence microscopy images showing HSN uptake (conc. 100 µg/mL) in hMSCs. Images are one Z stack selected based on the best resolution. Sidebars are cross sections in 3D constructed images from multiple Z-stack for each samples. Scale bar= 50 µm. N=3. Statistical significance of the concentration and DNA encapsulation effect are determined by comparing the uptake of each HSN formulation at 10 and 100 µg/mL and each HSN pair (eg cHSN and cHSN_D), respectively, where *p<0.01, **p<0.001 and ***p<0.0001. Error bars are derived from SD of biological triplicates.

to 300 µg/mL of Cu-HSN and Cu-HSN_D, hMSCs metabolism dropped to as low as 14.4 ± 4.0%, and 11.7 ± 17.9%, respectively (Figure 7a). This is likely due to degradation of the HSN framework and expulsion of Cu ions, which can induce cell autophagy and apoptosis (cuprotoxis).^{57,58}

Flow cytometry was also used to compare the intracellular uptake of different HSN formulations in hMSCs. We used two HSN incubation concentrations; 10 µg/mL and 100 µg/mL. At 10 µg/mL, there were little differences in hMSCs uptake of HSN. We observed that 9.8 ± 1.3% of hMSCs had taken up cHSN after 24 h, which was not different from the uptake of all other HSN formulations except for Sr-HSN and Se-HSN_D which were internalized significantly more ($p = 0.0259$ and $p = 0.0002$, respectively, Figure 7c). When HSN concentration was increased to 100 µg/mL, a significant increase in hMSCs uptake was observed for all formulations except Sr-HSN_D and Zn-HSN (Figure 7c). Further, differences in hMSCs uptake of HSN were observed at 100 µg/mL that were not present at 10 µg/mL likely due to the increased hMSCs fluorescence and enhanced resolution due to its logarithmic grading in flow cytometry.⁵⁹ Specifically, we observed that DNA-encapsulated HSN were taken up less by hMSCs than HSN (Figure 7c). We also observed that HSN uptake in hMSCs was dependent on the nature of the dopant ion. For example, the lowest uptake was observed when hMSCs were incubated with Zn-HSN and Zn-HSN_D (~15.1 ± 2.0%) while, Sr-HSN and Se-HSN_D were taken up the most (~68.1 ± 2.3%, $p < 0.0001$, Figure 7c, S12). A similar uptake trend for the different ion doped HSN at the concentration of 100 µg/mL was observed using fluorescent microscopy (Figure 7d). Furthermore, HSN internalization was evident in 3D cross sections constructed from multiple Z-stacks by the close proximity of HSN to the nuclei and actin filaments (Figure 7d). HSN distribution pattern around cell nuclei was similar between HSNs, where Se-HSN uptake was the highest, in line with our flow cytometry data.

Doping NP with different ions has been shown to lead to differential protein absorption.^{60,61} For example, Wang et al, demonstrated that quantum dots doped with 10 mol % Zn²⁺ showed a higher affinity for proteins than un-doped quantum dots. Increased protein absorption at the surface of silica NPs has been shown to reduce NP toxicity but disrupt cell uptake,^{62,63} likely due to the weakened interaction of NP with lipid membranes.⁶⁴ As such, we hypothesize that our ion doped HSN likely form different protein coronas in cell culture media, which caused variable hMSCs uptake.

Conclusions and Future Outlook

In summary, here we used a facile one-pot strategy to construct fluorescent, ion-doped hollow carriers that could efficiently encapsulate ON. Specifically, the HSN systems were efficiently dual doped with RITC and Ca²⁺, Cu²⁺, Zn²⁺, Se²⁺, or Sr²⁺ ions. Controlled ON release was observed from our HSNs over a 3 d period in GSH-rich intracellular conditions and limited release in the absence of GSH. Internalization of all our HSN formulations in hMSC was observed, where Ca-HSN, Zn-HSN, Se-HSN, and Sr-HSN remained non-toxic up to high concentrations.

The entrapment of ON in the core of HSN protects it from degradation, premature release, and enables efficient uptake in cells; representing a simple solution for current major challenges in the field of the gene delivery. Further, their facile one-pot synthesis has the potential to reduce costs associated with large scale production. Next to that, the developed HSNs have high potential to be used in various biomedical application via co-delivery of both ON and the incorporated ions, since slow HSN degradation was observed in intracellular conditions. Several of the ions used in this study have been associated with improved gene therapy outcomes by stimulating multiple biological processes simultaneously. For example, HANP gene vectors have been previously demonstrated to deliver both osteogenic ion Ca²⁺ as well as ON designed to lead to the production of osteogenic proteins (BMP), and their combination led to enhanced bone formation.⁶⁵⁻⁶⁷ Similarly, the developed cytotoxic Cu-HSN could be used to co-deliver Cu²⁺ and ON to improved anti-cancer efficacy. Such strategies have been reported previously, where compared to ON alone, enhanced tumor immunogenicity, growth suppression, was observed when Cu²⁺ was co-delivered.⁶⁸⁻⁷⁰

Due to the one-pot synthetic procedure, our bioactive ion doped HSN can be easily tailored for a range of gene therapeutic applications simply by incorporating different ON in-situ. For example, our Ca-HSN, Zn-HSN, and Sr-HSN containing osteoinductive Ca²⁺, Sr²⁺, and Zn²⁺ could incorporate ON designed to induce osteogenesis for new bone formation, while HSN doped with cytotoxic Cu²⁺ or Se²⁺ could load ON encoded to induce apoptosis for oncological applications. ON can also be modified to enhance their stability and DNA binding affinity⁷¹ which, in combination with our HSN systems, is a promising strategy to provide robust protection against both nuclease degradation and hydrolysis of ON. Further, larger therapeutics such as enzymes, antibodies and nucleases could be entrapped in our HSN and the

surface could also be modified to enable subcellular targeting or prolonged cargo release. Overall, we propose our fluorescent, ion-doped HSN as adaptable ON delivery platforms that can be easily tailored for a vast array of gene therapy applications from chemotherapy to tissue regeneration.

Data Sharing Statement

All data recorded for this project is presented in this manuscript and [the supplementary information](#).

Acknowledgments

The authors would like to acknowledge the Netherlands Organization for Health Research and Development for funding (ZonMw TOP, grant number; 91217058). The authors would also like to acknowledge H. Duimel and the Maastricht Multimodal Molecular Imaging Institute (M4I) for help with EDX measurements and sample preparation.

Disclosure

The authors declare that they have no known competing financial interests or personal relationships that could have influenced the work reported in this paper.

References

1. Khvorova A, Watts JK. The chemical evolution of oligonucleotide therapies of clinical utility. *Nat Biotechnol.* 2017;35(3):238–248. doi:10.1038/nbt.3765
2. Shih PC, Naganuma M, Demizu Y, Naito M. Current Status of Oligonucleotide-Based Protein Degradation. *Pharmaceutics.* 2023;15(3). doi:10.3390/pharmaceutics15030765
3. Quemener AM, Galibert MD. Antisense oligonucleotide: a promising therapeutic option to beat COVID-19. *Wiley Interdiscip Rev RNA.* 2022;13(4):e1703. doi:10.1002/wrna.1703
4. Thomas CE, Ehrhardt A, Kay MA. Progress and problems with the use of viral vectors for gene therapy. *Nat Rev Genet.* 2003;4(5):346–358. doi:10.1038/nrg1066
5. Mendes BB, Connot J, Avital A, et al. Nanodelivery of nucleic acids. *Nat Rev Meth Primers.* 2022;2(1):24.
6. Hosseinpour S, Cao Y, Liu J, Xu C, Walsh LJ. Efficient transfection and long-term stability of rno-miRNA-26a-5p for osteogenic differentiation by large pore sized mesoporous silica nanoparticles. 10.1039/D0TB02756A. *J Mater Chem B.* 2021;9(9):2275–2284. doi:10.1039/d0tb02756a
7. Kim T-H, Singh RK, Kang MS, Kim J-H, Kim H-W. Gene delivery nanocarriers of bioactive glass with unique potential to load BMP2 plasmid DNA and to internalize into mesenchymal stem cells for osteogenesis and bone regeneration. 10.1039/C5NR07933K. *Nanoscale.* 2016;8(15):8300–8311. doi:10.1039/c5nr07933k
8. Luo D, Xu X, Iqbal MZ, et al. siRNA-Loaded Hydroxyapatite Nanoparticles for KRAS Gene Silencing in Anti-Pancreatic Cancer Therapy. *Pharmaceutics.* 2021;13(9):1428. doi:10.3390/pharmaceutics13091428
9. Dördelmann G, Kozlova D, Karczewski S, Lizio R, Knauer S, Epple M. Calcium phosphate increases the encapsulation efficiency of hydrophilic drugs (proteins, nucleic acids) into poly(D,L-lactide-co-glycolide acid) nanoparticles for intracellular delivery. 10.1039/C4TB00922C. *J Mater Chem B.* 2014;2(41):7250–7259. doi:10.1039/c4tb00922c
10. Chang F-P, Hung Y, Chang J-H, Lin C-H, Mou C-Y. Enzyme Encapsulated Hollow Silica Nanospheres for Intracellular Biocatalysis. *ACS Appl Mater Interfaces.* 2014;6(9):6883–6890. doi:10.1021/am500701c
11. Chang F-P, Chen Y-P, Mou C-Y. Intracellular Implantation of Enzymes in Hollow Silica Nanospheres for Protein Therapy: cascade System of Superoxide Dismutase and Catalase. *Small.* 2014;10(22):4785–4795.
12. S-M J, Jiang S, Graf R, Wurm FR, Landfester K. Aqueous core and hollow silica nanocapsules for confined enzyme modules. 10.1039/D0NR07148J. *Nanoscale.* 2020;12(47):24266–24272. doi:10.1039/d0nr07148j
13. Ma X, Zhao Y, Ng KW, Zhao Y. Integrated hollow mesoporous silica nanoparticles for target drug/siRNA co-delivery. *Chem Eur J.* 2013;19(46):15593–15603. doi:10.1002/chem.201302736
14. Lin X, Wu M, Li M, et al. Photo-responsive hollow silica nanoparticles for light-triggered genetic and photodynamic synergistic therapy. *Acta Biomater.* 2018;76:178–192. doi:10.1016/j.actbio.2018.07.007
15. Trayford C, Wilhelm A, Habibovic P, Smeets H, van Tienen F, van Rijt S. One-pot, degradable, silica nanocarriers with encapsulated oligonucleotides for mitochondrial specific targeting. *Discover Nano.* 2023;18(1):161. doi:10.1186/s11671-023-03926-1
16. Shen Y, Shao Y, He H, et al. Gadolinium(3+)-doped mesoporous silica nanoparticles as a potential magnetic resonance tracer for monitoring the migration of stem cells in vivo. *Int J Nanomed.* 2013;8:119–127. doi:10.2147/IJN.S38213
17. Liu X, Sun Y, Shen J, Min HS, Xu J, Chai Y. Strontium doped mesoporous silica nanoparticles accelerate osteogenesis and angiogenesis in distraction osteogenesis by activation of Wnt pathway. *Nanomed Nanotechnol Biol Med.* 2022;41:102496.
18. Wang X, Li X, Ito A, et al. Biodegradable Metal Ion-Doped Mesoporous Silica Nanospheres Stimulate Anticancer Th1 Immune Response in Vivo. *ACS Appl Mater Interfaces.* 2017;9(50):43538–43544. doi:10.1021/acsami.7b16118
19. He L, Habibovic P, van Rijt S. Selenium-incorporated mesoporous silica nanoparticles for osteosarcoma therapy. 10.1039/D2BM02102A. *Biomater Sci.* 2023;11(11):3828–3839. doi:10.1039/d2bm02102a
20. Ma H, Ma Z, Chen Q, et al. Bifunctional, Copper-Doped, Mesoporous Silica Nanosphere-Modified, Bioceramic Scaffolds for Bone Tumor Therapy. *Origin Res Front Chem.* 2020;8.

21. Choi E, Lim D-K, Kim S. Calcium-doped mesoporous silica nanoparticles as a lysosomolytic nanocarrier for amine-free loading and cytosolic delivery of siRNA. *J Ind Eng Chem.* 2020;81:71–80.
22. Lee JE, Lee N, Kim H, et al. Uniform Mesoporous Dye-Doped Silica Nanoparticles Decorated with Multiple Magnetite Nanocrystals for Simultaneous Enhanced Magnetic Resonance Imaging, Fluorescence Imaging, and Drug Delivery. *J Am Chem Soc.* 2010;132(2):552–557.
23. Goh Y-F, Alshemary AZ, Akram M, Abdul Kadir MR, Hussain R. Bioactive Glass: an In-Vitro Comparative Study of Doping with Nanoscale Copper and Silver Particles. *Int J Appl Glass Sci.* 2014;5(3):255–266.
24. Moran CE, Hale GD, Halas NJ. Synthesis and Characterization of Lanthanide-Doped Silica Microspheres. *Langmuir.* 2001;17(26):8376–8379.
25. Corrales LR, Park B. Molecular dynamics simulation of La₂O₃–Na₂O–SiO₂ glasses. III. The driving forces of clustering. *J Non-Cryst Solids.* 2002;311(2):118–129.
26. Bochkova O, Khrizanforov M, Gubaidullin A, et al. Synthetic Tuning of CoII-Doped Silica Nanoarchitecture Towards Electrochemical Sensing Ability. *Nanomaterials.* 2020;10(7):1338. doi:10.3390/nano10071338
27. Yoo H, Pak J. Synthesis of highly fluorescent silica nanoparticles in a reverse microemulsion through double-layered doping of organic fluorophores. *J Nanopart Res.* 2013;15(5):1609.
28. Karaer E, Köse DA, Şahin Z S, Şahin O. Novel coordination compounds of alkaline earth metals with coumarilic acid. Synthesis and characterization. *J Molecular Sci.* 2021;1244:130970.
29. Burgess KMN, Xu Y, Leclerc MC, Bryce DL. Alkaline-Earth Metal Carboxylates Characterized by ⁴³Ca and ⁸⁷Sr Solid-State NMR: impact of Metal-Amine Bonding. *Inorg Chem.* 2014;53(1):552–561.
30. Bala T, Prasad BL, Sastry M, Kahaly MU, Waghmare UV. Interaction of different metal ions with carboxylic acid group: a quantitative study. *J Phys Chem A.* 2007;111(28):6183–6190. doi:10.1021/jp067906x
31. Ma ZY, Dosev D, Kennedy IM. A microemulsion preparation of nanoparticles of europium in silica with luminescence enhancement using silver. *Nanotechnology.* 2009;20(8):085608. doi:10.1088/0957-4484/20/8/085608
32. Mukhametshina AR, Mustafina AR, Davydov NA, et al. Tb(III)-Doped Silica Nanoparticles for Sensing: effect of Interfacial Interactions on Substrate-Induced Luminescent Response. *Langmuir.* 2015;31(1):611–619. doi:10.1021/la503074p
33. Sharma P, Bengtsson NE, Walter GA, et al. Gadolinium-Doped Silica Nanoparticles Encapsulating Indocyanine Green for Near Infrared and Magnetic Resonance Imaging. *Small.* 2012;8(18):2856–2868. doi:10.1002/sml.201200258
34. Ashoka AH, Aparin IO, Reisch A, Klymchenko AS. Brightness of fluorescent organic nanomaterials. 10.1039/d2cs00464j. *Chem Soc Rev.* 2023;52(14):4525–4548. doi:10.1039/d2cs00464j
35. Polyanichko AM, Chikhirzhina EV, Andrushchenko VV, Kostyleva EI, Wieser H, Vorob'ev VI. The Effect of Ca²⁺ Ions on DNA Compaction in the Complex with HMGB1 Nonhistone Chromosomal Protein. *Molecular Biol.* 2004;38(4):590–600.
36. Süleymanoğlu E. Mg²⁺-induced DNA compaction, condensation, and phase separation in gene delivery vehicles based on zwitterionic phospholipids: a dynamic light scattering and surface-enhanced Raman spectroscopic study. *J Biol Inorg Chem.* 2017;22(8):1165–1177. doi:10.1007/s00775-017-1492-x
37. Islam MM, Chakraborty M, Pandya P, Al Masum A, Gupta N, Mukhopadhyay S. Binding of DNA with Rhodamine B: spectroscopic and molecular modeling studies. *Dyes Pigm.* 2013;99(2):412–422.
38. Nguyen L, Döblinger M, Liedl T, Heuer-Jungemann A. DNA-Origami-Templated Silica Growth by Sol–Gel Chemistry. *Angew Chem Int Ed.* 2019;58(3):912–916.
39. Nguyen M-K, Nguyen VH, Natarajan AK, et al. Ultrathin Silica Coating of DNA Origami Nanostructures. *Chem Mater.* 2020;32(15):6657–6665.
40. Korolev N, Lyubartsev AP, Rupprecht A, Nordenskiöld L. Competitive Binding of Mg²⁺, Ca²⁺, Na⁺, and K⁺ Ions to DNA in Oriented DNA Fibers: experimental and Monte Carlo Simulation Results. *Biophys J.* 1999;77(5):2736–2749. doi:10.1016/s0006-3495(99)77107-9
41. Hackl EV, Kornilova SV, Kapinos LE, et al. Study of Ca²⁺, Mn²⁺ and Cu²⁺ binding to DNA in solution by means of IR spectroscopy. *J Molecular Sci.* 1997;408-409:229–232.
42. Shi M, Chen Z, Farnaghi S, et al. Copper-doped mesoporous silica nanospheres, a promising immunomodulatory agent for inducing osteogenesis. *Acta Biomater.* 2016;30:334–344. doi:10.1016/j.actbio.2015.11.033
43. Wu W, Ngo A, Ban W, et al. Tailoring head–tail mesoporous silica nanoparticles for enhanced gene transfection. 10.1039/d2tb01737g. *J Mater Chem B.* 2022;10(39):7995–8002. doi:10.1039/d2tb01737g
44. Zhang W, Kang X, Yuan B, et al. Nano-Structural Effects on Gene Transfection: large, Botryoid-Shaped Nanoparticles Enhance DNA Delivery via Macropinocytosis and Effective Dissociation. *Theranostics.* 2019;9(6):1580–1598. doi:10.7150/thno.30302
45. Ainalem ML, Bartles A, Muck J, et al. DNA compaction induced by a cationic polymer or surfactant impact gene expression and DNA degradation. *PLoS One.* 2014;9(3):e92692. doi:10.1371/journal.pone.0092692
46. Pohaku Mitchell KK, Liberman A, Kummel AC, Trogler WC. Iron(III)-Doped, Silica Nanoshells: a Biodegradable Form of Silica. *J Am Chem Soc.* 2012;134(34):13997–14003. doi:10.1021/ja3036114
47. Önem AN, Sözgen Başkan K, Apak R. Voltammetric Measurement of Antioxidant Activity by Prevention of Cu(II)-Induced Oxidative Damage on DNA Bases Using a Modified Electrode. *ACS Omega.* 2023;8(5):5103–5115. doi:10.1021/acsomega.2c08055
48. He Q, Shi J, Zhu M, Chen Y, Chen F. The three-stage in vitro degradation behavior of mesoporous silica in simulated body fluid. *Microporous Mesoporous Mater.* 2010;131(1):314–320.
49. Giovaninni G, Moore CJ, Hall AJ, Byrne HJ, Gubala V. pH-Dependent silica nanoparticle dissolution and cargo release. *Colloids Surf B Biointerfaces.* 2018;169:242–248. doi:10.1016/j.colsurfb.2018.04.064
50. Vandenbroucke RE, De Geest BG, Bonné S, et al. Prolonged gene silencing in hepatoma cells and primary hepatocytes after small interfering RNA delivery with biodegradable poly(β-amino esters). *J Gene Med.* 2008;10(7):783–794. doi:10.1002/jgm.1202
51. Dobek GL, Zhang X, Balazs DA, Godbey WT. Analysis of promoters and expression-targeted gene therapy optimization based on doubling time and transfectability. *FASEB J.* 2011;25(9):3219–3228. doi:10.1096/fj.11-185421
52. Rodriguez Ramos A, Marin L, Iturrioz N, et al. Design of Polymeric and Biocompatible Delivery Systems by Dissolving Mesoporous Silica Templates. *Int J Mol Sci.* 2020;21. doi:10.3390/ijms21249573
53. Choi E, Kim S. Surface pH buffering to promote degradation of mesoporous silica nanoparticles under a physiological condition. *J Colloid Interface Sci.* 2019;533:463–470. doi:10.1016/j.jcis.2018.08.088

54. Tang H, Li C, Zhang Y, et al. Targeted Manganese doped silica nano GSH-cleaner for treatment of Liver Cancer by destroying the intracellular redox homeostasis. *Theranostics*. 2020;10(21):9865–9887. doi:10.7150/thno.46771
55. Hao X, Hu X, Zhang C, et al. Hybrid Mesoporous Silica-Based Drug Carrier Nanostructures with Improved Degradability by Hydroxyapatite. *ACS Nano*. 2015;9(10):9614–9625. doi:10.1021/nn507485j
56. Forman HJ, Zhang H, Rinna A. Glutathione: overview of its protective roles, measurement, and biosynthesis. *Mol Asp Med*. 2009;30(1–2):1–12.
57. Anjos VA, da Silva- JFMR, Souza MM. Cell damage induced by copper: an explant model to study anemone cells. *Vitro Toxicol*. 2014;28(3):365–372.
58. Mancuso L, Cao G. Acute toxicity test of CuO nanoparticles using human mesenchymal stem cells. *Toxicol Mech Meth*. 2014;24(7):449–454.
59. Schmid I, Schmid P, Giorgi JV. Conversion of logarithmic channel numbers into relative linear fluorescence intensity. *Cytometry*. 1988;9(6):533–538. doi:10.1002/cyto.990090605
60. Ciobanu V, Roncari F, Ceccone G, et al. Protein-Corona formation on aluminum doped zinc oxide and gallium nitride nanoparticles. *J Appl Bio Mater*. 2022;20:22808000221131881.
61. Wang J, Yang B, Yu X, Chen S, Li W, Hong X. The impact of Zn doping on CdTe quantum dots-protein Corona formation and the subsequent toxicity at the molecular and cellular level. *Chem Biol Interact*. 2023;373:110370. doi:10.1016/j.cbi.2023.110370
62. Aliyandi A, Reker-Smit C, Bron R, Zuhorn IS, Salvati A. Correlating Corona Composition and Cell Uptake to Identify Proteins Affecting Nanoparticle Entry into Endothelial Cells. *ACS Biomater Sci Eng*. 2021;7(12):5573–5584. doi:10.1021/acsbomaterials.1c00804
63. Hayakawa N, Kitayama Y, Igarashi K, et al. Fc Domain-Imprinted Stealth Nanogels Capable of Orientational Control of Immunoglobulin G Adsorbed In Vivo. *ACS Appl Mater Interfaces*. 2022;14(14):16074–16081. doi:10.1021/acsaami.2c01953
64. Arribas Perez M, Beales PA. Protein Corona alters the mechanisms of interaction between silica nanoparticles and lipid vesicles. 10.1039/D2SM00739H. *Soft Matter*. 2022;18(27):5021–5026. doi:10.1039/d2sm00739h
65. Limlawan P, Marger L, Durual S, Vacharaksa A. Delivery of microRNA-302a-3p by APTES modified hydroxyapatite nanoparticles to promote osteogenic differentiation in vitro. *BDJ Open*. 2023;9(1):8. doi:10.1038/s41405-023-00135-x
66. Lee MC, Seonwoo H, Jang KJ, et al. Development of novel gene carrier using modified nano hydroxyapatite derived from equine bone for osteogenic differentiation of dental pulp stem cells. *Bioactive Mater*. 2021;6(9):2742–2751.
67. Khalifehzadeh R, Arami H. DNA-Templated Strontium-Doped Calcium Phosphate Nanoparticles for Gene Delivery in Bone Cells. *ACS Biomater Sci Eng*. 2019;5(7):3201–3211. doi:10.1021/acsbomaterials.8b01587
68. Ghasemi P, Shafiee G, Ziamajidi N, Abbasalipourkabir R. Copper Nanoparticles Induce Apoptosis and Oxidative Stress in SW480 human Colon Cancer Cell Line. *Biol Trace Elem Res*. 2023;201(8):3746–3754. doi:10.1007/s12011-022-03458-2
69. He H, Zou Z, Wang B, et al. Copper Oxide Nanoparticles Induce Oxidative DNA Damage and Cell Death via Copper Ion-Mediated P38 MAPK Activation in Vascular Endothelial Cells. *Int J Nanomed*. 2020;15:3291–3302.
70. Chen C, Ma Y, Du S, et al. Controlled CRISPR-Cas9 Ribonucleoprotein Delivery for Sensitized Photothermal Therapy. *Small*. 2021;17(33):2101155.
71. Kulkarni JA, Witzigmann D, Thomson SB, et al. The current landscape of nucleic acid therapeutics. *Nat Nanotechnol*. 2021;16(6):630–643. doi:10.1038/s41565-021-00898-0

International Journal of Nanomedicine

Dovepress

Publish your work in this journal

The International Journal of Nanomedicine is an international, peer-reviewed journal focusing on the application of nanotechnology in diagnostics, therapeutics, and drug delivery systems throughout the biomedical field. This journal is indexed on PubMed Central, MedLine, CAS, SciSearch®, Current Contents®/Clinical Medicine, Journal Citation Reports/Science Edition, EMBase, Scopus and the Elsevier Bibliographic databases. The manuscript management system is completely online and includes a very quick and fair peer-review system, which is all easy to use. Visit <http://www.dovepress.com/testimonials.php> to read real quotes from published authors.

Submit your manuscript here: <https://www.dovepress.com/international-journal-of-nanomedicine-journal>